

Decaying and decayless transverse oscillations of a coronal loop^{*}

G. Nisticò¹, V. M. Nakariakov^{1,2}, and E. Verwichte¹

¹ Centre for Fusion, Space and Astrophysics, Department of Physics, University of Warwick, CV4 7AL, UK
e-mail: g.nistico@warwick.ac.uk

² Central Astronomical Observatory at Pulkovo of the Russian Academy of Sciences, 196140 St Petersburg, Russia

Received 31 October 2012 / Accepted 30 January 2013

ABSTRACT

Aims. We investigate kink oscillations of loops observed in an active region with the Atmospheric Imaging Assembly (AIA) instrument on board the Solar Dynamics Observatory (SDO) spacecraft before and after a flare.

Methods. The oscillations were depicted and analysed with time-distance maps, extracted from the cuts taken parallel or perpendicular to the loop axis. Moving loops were followed in time with steadily moving slits. The period of oscillations and its time variation were determined by best-fitting harmonic functions.

Results. We show that before and well after the occurrence of the flare, the loops experience low-amplitude decayless oscillations. The flare and the coronal mass ejection associated to it trigger large-amplitude oscillations that decay exponentially in time. The periods of the kink oscillations in both regimes (about 240 s) are similar. An empirical model of the phenomenon in terms of a damped linear oscillator excited by a continuous low-amplitude harmonic driver and by an impulsive high-amplitude driver is found to be consistent with the observations.

Key words. Sun: corona – Sun: oscillations – methods: observational

1. Introduction

Transverse, or kink, oscillations of solar coronal loops are among the most often studied dynamical phenomena in the corona since their discovery (Aschwanden et al. 1999; Nakariakov et al. 1999) with the Transition Region and Coronal Explorer (TRACE; Handy et al. 1999). These oscillations are confidently detected with high-resolution extreme ultra-violet (EUV) imagers, such as the Atmospheric Imaging Assembly (AIA) on board the Solar Dynamics Observatory (SDO; Lemen et al. 2012), and before they were discovered, they were the subject of theoretical and numerical studies (e.g. Edwin & Roberts 1983; Roberts et al. 1984; Murawski & Roberts 1994). The common observational manifestation of transverse oscillations are flare-generated rapidly decaying standing global modes (e.g. Nakariakov et al. 1999) or higher spatial harmonics (Verwichte et al. 2004; De Moortel & Brady 2007; Van Doorselaere et al. 2007), but they have been observed as propagating waves in quiescent active regions (Tomczyk et al. 2007) and in supra-arcades of flaring arcades (Verwichte et al. 2005). Typical periods of kink oscillations range from a few minutes to several hours (e.g. Verwichte et al. 2010; White & Verwichte 2012; the latter case corresponds to cool fibrils of quiescent prominences, see Hershaw et al. 2011). In terms of magnetohydrodynamic (MHD) wave theory kink oscillations are interpreted as kink ($m = 1$) fast magnetoacoustic modes (e.g. Edwin & Roberts 1983; Van Doorselaere et al. 2008), which become weakly compressible in the long-wavelength limit (Goossens et al. 2012).

The interest in kink oscillations of coronal loops is mainly connected with their use as a seismological probe of the abso-

lute value of the magnetic field (Nakariakov & Ofman 2001), and also with their peculiarly rapid damping after excitation (e.g. Ruderman & Roberts 2002; Goossens et al. 2002). It has been demonstrated that the damping can be caused by resonant absorption, that is, linear coupling of the kink oscillations with unresolved torsional motions. Standing kink oscillations can be excited by an impulsive, flare-generated driver (e.g. McLaughlin & Ofman 2008), by a periodic driver associated with a coronal wave (Ballai et al. 2008; Selwa et al. 2010), or directly from reconnection (White et al. 2012). Alternative mechanisms, e.g. the effect of Alfvénic vortex shedding (e.g. Nakariakov et al. 2009) are also considered. Moreover propagating kink waves show rapid decay with height, which is believed to be consistent with the resonant absorption theory (Terradas et al. 2010; Pascoe et al. 2010; Verth et al. 2010). Verifying the theories requires detailed, high-precision observations of this phenomenon.

In this work we present an observation of two different regimes of transverse oscillations, low-amplitude decayless and high-amplitude decaying, in the same EUV loop.

2. Observations

The analysed coronal loops were observed on the south-eastern solar limb on 30 May, 2012, between 08:00–11:00 UT with AIA on board SDO, which provides full-disk images of the Sun at different EUV wavelengths at high spatial resolution (1 pixel \approx 0.6 arcsec) every 12 s for each bandpass. The loop plane is almost parallel to the line-of-sight. The loops were visible in almost all six EUV wavelengths: their appearance is weak at 94 and 335 Å, while in 131, 171, 193, and 211 Å they are clearly visible (better at 171 and 193 Å). This indicates that the loops have a thermal distribution of about 0.8 and 2 MK. The system of multi-thermal coronal loops belongs to

^{*} Two movies are available in electronic form at <http://www.aanda.org>

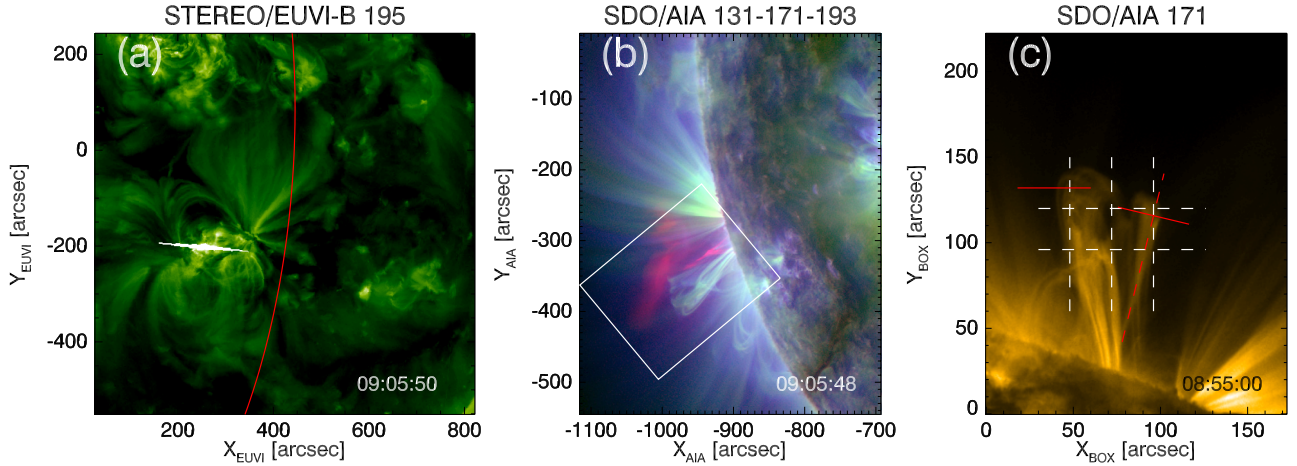


Fig. 1. **a)** Image of the AR NOAA 11494 and the flare from STEREO/EUVI-B at 195 Å: the red line marks the position of the solar limb as seen from SDO (or Earth). **b)** RGB (red, green, blue) image of 131, 171, and 193 Å snapshots from SDO at the time of the flare: the release of the plasma bubble after the flare is visible in the red (131) channel. **c)** Adaptation of the white rectangle in **b)** at 171 Å showing the loop system with the overplotted slits (white and red continuous lines). The movie available on-line shows the temporal evolution of the RGB image of the white rectangle in panel **b)** and the time evolution of panel **c)**. The movie also contains the time-distance maps shown in Fig. 3.

the active region (AR) NOAA 11494, which was still behind the solar limb at the time of the observations and emerged only two days later, additionally exhibiting a sunspot. The AR was also visible from the Extreme Ultra Violet Imager (EUVI) of the Solar TERrestrial RELation Observatory (STEREO)-B, which was distant by a few degrees from the solar limb, as seen from the Earth perspective (the red line in Fig. 1a). We cannot appreciate all fine details as seen from SDO, since the spatial resolution is lower (1 pixel \approx 1.6 arcsec), and the identifications of the same loops are quite difficult at 195 Å (plasma temperature response \approx 1.5 MK). At the time of the observations, a flare occurred in the AR: the typical bright breadth of pixels saturated in intensity was recorded at 09:05 UT in EUVI-B. The GOES observatories registered a flare of class C1.0 during the time interval 08:36–09:07 UT. Several minutes later, post-flare loops developed at the right side of the loop system, and they were visible at EUV wavelengths. A view from SDO is given in Fig. 1b: we combined three different EUV bandpasses, 131, 171, and 193 Å, respectively in the red, green, and blue (RGB) channels of the image. This allows us to depict the plasma dynamics at different temperature ranges. The response functions of the 171 and 193 filters show peaks around 1 MK, while the 131 channel has a response function peaking at 0.5 MK and 10 MK. While loops are better visible in the first two filters, the flare is clearly observed at 131 Å, as well as the release of the plasma bubble, that looks a coronal mass ejection (CME). This release is also recorded in the hot channels at 94 and 335 Å (but in the latter case it is not seen in “emission”), indicating that the plasma is probably heated at temperatures around \sim 10 MK. The coronal loops are enclosed inside the white box, and an adaptation of it is shown in Fig. 1c at 171 Å, a few minutes before the flare. When the flare occurs, transverse oscillations of the loops are triggered, which decay within about 20 min. Moreover, a careful inspection of the loops shows that transverse oscillations of smaller amplitude are present before the flare and also after the impulsive event (see movie on-line). Furthermore, a loop at the right side of the system is increasing its height in time, clearly showing small-amplitude oscillations before the flare. Here, we focus on the AIA 171 Å dataset. We selected a box containing the loops that has vertices (starting from the left bottom corner) of coordinates

$[(-947.1, -1036.5), (-1118.1, -1179.3), (-1228.5, -1046.1), (-1057.5, -903.3)]$ arcsec: the box is 172.8 arcsec wide and 222.6 arcsec high. We extracted it from the full images, straightened them up as in Fig. 1c, and analysed them.

3. Analysis and results

To study the transverse oscillations, we took slits more or less parallel and perpendicular to the loop plane and 11-pixel-wide (white lines in Fig. 1c), at positions $X_{\text{BOX}} = 48, 72, 96$ arcsec, and $Y_{\text{BOX}} = 96, 120$ arcsec, in a similar way as in previous works (e.g. Verwichte et al. 2004; Hershaw et al. 2011; White & Verwichte 2012). We calculated a mean value over the width at every position along the slit to increase the signal-to-noise ratio. By stacking slits at every time step (every \sim 12 s), we created time-distance plots, that show the intensity variation in time along the slit (Fig. 2). A decaying wave-like pattern is evident, indicating a periodic displacement of the loop after the flare, whose time is marked with a white dashed line. At first glance we can note that some static bright features are present as well, which suggests that some loops do not oscillate (or maybe have small-amplitude oscillations that are not resolved). In Figs. 2a, b, we see that the oscillations are more pronounced at higher distance from the footpoints, indicating that the loop tops oscillate more than the middle part. A similar behaviour was found for the horizontal slits (Fig. 2c), whose amplitude is larger at the right side (top oscillations in the time-distance maps) of the loop system (also closer to the flare site). The CME related to these oscillations shows a speed estimated to be more than 450 km s^{-1} from AIA-131 data. In addition, decayless oscillations with smaller amplitudes are displayed 30 min before and after the flare (e.g. see Figs. 2a–c). Time series of the loop displacement were extracted from the time-distance maps with a Gaussian fit of the intensity profile or by eye inspection, and were fitted with the function

$$y(t) = \xi \cos\left(\frac{2\pi(t - t_0)}{P} - \phi\right) \exp\left(-\frac{t - t_0}{\tau}\right) + f(t), \quad (1)$$

where $f(t)$ is a steady trend (typically linear) in the loop displacement ($f(t) = y_0 + v_0(t - t_0)$). Parameters estimated from the

Table 1. Fitting parameters of transverse loop oscillations.

Event	ξ [Mm]	P [s]	ϕ [deg]	τ [s]	v_0 [km s ⁻¹]	χ^2
x_1	0.49 ± 0.19	312.95 ± 11.30	166.06 ± 40.29		1.5 ± 0.24	5.40
x_2	0.093 ± 0.58	196.44 ± 70.23	170.94 ± 587.35		0.37 ± 0.75	0.30
x_3	4.07 ± 1.90	254.63 ± 11.74	28.84 ± 28.02	532.54 ± 312.94	2.8 ± 0.41	3.11
y_1	0.20 ± 0.34	332.81 ± 121.08	95.51 ± 170.60		2.2 ± 0.97	0.69
y_2	2.28 ± 0.62	208.83 ± 7.82	17.84 ± 18.23	511.36 ± 265.35	1.7 ± 0.69	13.02

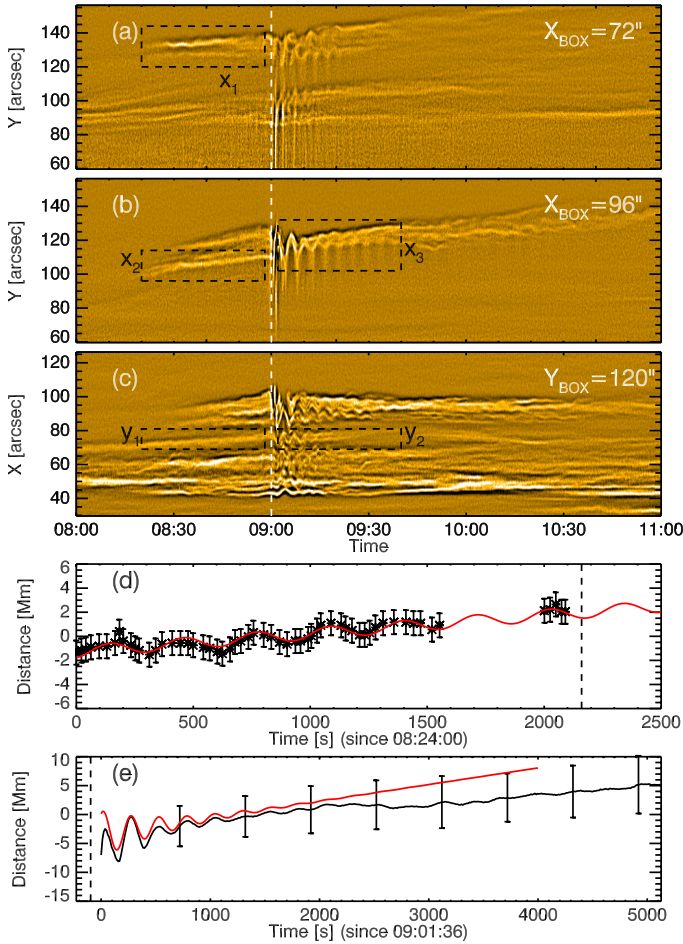


Fig. 2. High-pass-filtered time-distance maps **a)–c)** obtained from the slits. Transverse oscillations are enclosed by the black dashed boxes. Time series plots **d)–e)** and associated fits (red lines) for events x_1 , and x_3 . The white (black) dashed lines in the time-distance maps (time series plots) represent the time of the flare.

fits are reported in Table 1. The typical oscillation period ranges between 200–300 s (Figs. 2d, e, Table 1), and the decay time is about 500 s. This ratio of the period to the decay time is typical for decaying kink oscillations (e.g. White & Verwichte 2012).

To take into account the variation in size of the loops and their direction, we focused on the expanding loop at the right of the system: we took a slit located at the top of the loop and moved with it (slanted red line in Fig. 1c, the path is marked by a dashed red line). We distinguish three different phases (low-large-low amplitude oscillations, which show decayless-decaying-decayless behaviour). The slit during the first phase was moved faster (the speed of the expanding loop is estimated to be about 10 km s⁻¹) than in the second, and in the last phase it was kept stable since the loop height did not seem to change

considerably (see on-line movie). We compared this also with another slit (located at $Y_{\text{BOX}} = 132$ arcsec; the red slit at the left side in Fig. 1c). A picture of the time-distance maps obtained is given in Fig. 3 (top). A running difference of five frames was subtracted from the signal to highlight the oscillations: a pattern with recurring dark and bright spots was obtained by this operation. We also analysed the period changes in time by counting the maxima (red bullet) and minima (blue bullet) in the intensity profile, taken at a specific cut in the time-distance maps (Fig. 3, middle). We estimated the period by evaluating the time between the consecutive maxima (or minima) peaks. Scatter plots of the measured period in time are given in Fig. 3 (bottom). For the moving slit, we note that the period is initially about 200 s, then it abruptly increases to 300 s (possibly because of the interaction with another loop at 193 Å), then decreases and again increases to 300 s during the large-amplitude phase. A similar behaviour is noted in the third phase, when the loop height is higher than in the first case. From the right scatter plot (fixed slit), no clear trend for the period evolution can be inferred: the scatter of data is larger than in the previous one, and the average period is 224.19 s.

We estimated the magnitude of the magnetic field with coronal seismology. The length of the loops is inferred by considering the two views from STEREO-B and SDO to determine the “true” length and not just the projection on the plane of sight. In addition, we used difference images to recognise by eye the brightness variation and associated them to the same loop (see on-line movie). In a similar way as in Verwichte et al. (2010), we calculated the positions of the loop by identifying the footpoints in EUVI-B, and compared the 3D positions resulting from the `scc_measure.pro` with a semi-elliptical profile, which matches the loop shape well. The results are given in Fig. 4.

By knowing the loop length and the period, we can estimate the phase speed (or kink speed), and consequently the Alfvén speed, as

$$C_K = \sqrt{\frac{2}{1 + \frac{\rho_e}{\rho_0}}} V_{A0} \approx \frac{2L}{P}, \quad (2)$$

with ρ_e and ρ_0 the external and internal density, and V_{A0} the internal Alfvén speed. Since the density contrast can change between 0 and 1, the Alfvén speed will range between a lower and an upper limit: $2L/(\sqrt{2}P) \leq V_{A0} \leq 2L/P$. On the other hand, the magnetic field is expressed as (in *cgs* units)

$$B = V_A \sqrt{4\pi\mu_C m_p n_e}, \quad (3)$$

with μ_C the mean molecular weight in the corona, which is equal to 1.27, m_p is the proton mass, and n_e the electron density. From the value range of the Alfvén speed, the corresponding magnetic field is estimated as (see Nakariakov & Ofman 2001; White & Verwichte 2012)

$$\frac{2L}{\sqrt{2}P} \sqrt{\mu_C m_p n_e} \leq B \leq \frac{2L}{P} \sqrt{\mu_C m_p n_e}. \quad (4)$$

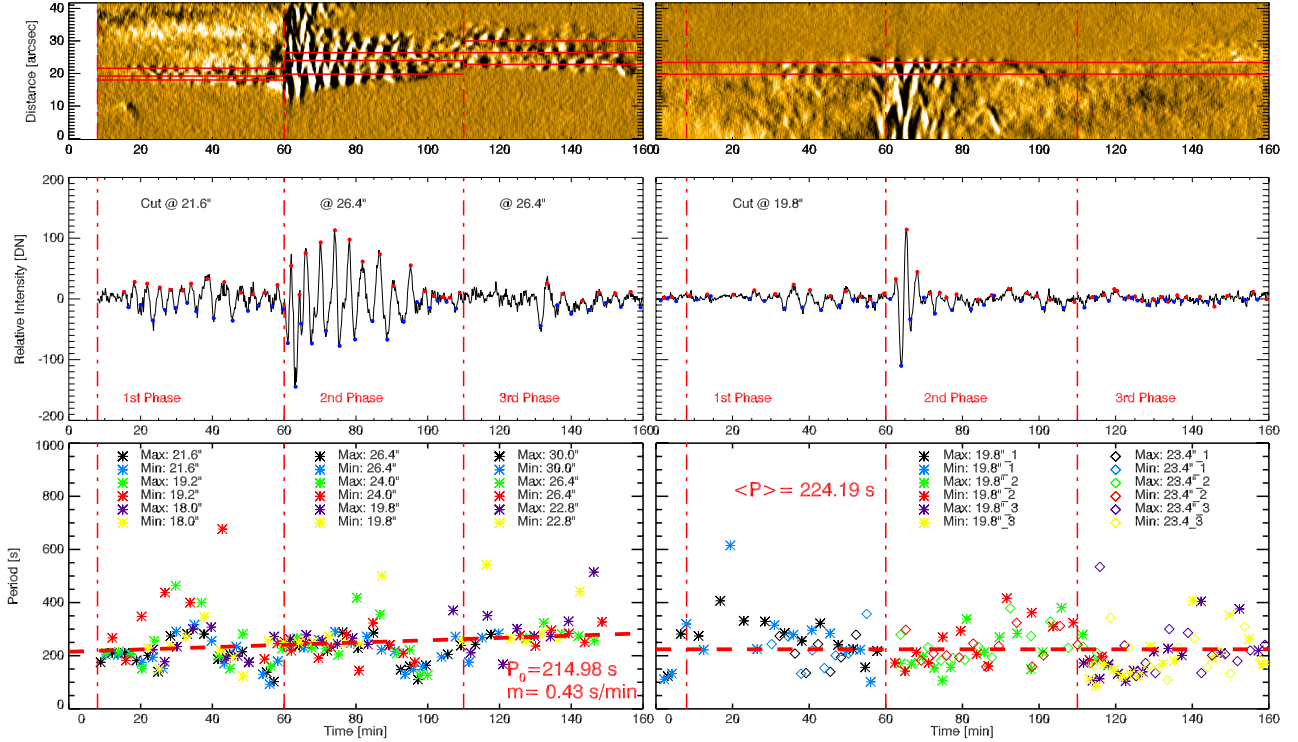


Fig. 3. *Top:* time-distance maps for the moving (*left panel*) and steady (*right panel*) slit (red lines in Fig. 1c). The time distance map of *the top left panel* is included in the on-line movie; it shows the loop evolution. *Middle:* zoomed parts of the time-distance maps: the red and blue bullets are the maxima and minima positions. *Bottom:* period vs. time as inferred from the intensity profiles above (red lines in the time-distance maps). The vertical dot-dashed lines show the different oscillation regimes. The dashed line shows the linear trend in the period, with the initial value about 214 s and the increment of 0.43 s/min (*left panel*), and the average period of 224.19 s (*right panel*).

Table 2. Seismological diagnostic.

Loop	Length [Mm]	θ [deg]	δ [deg]	P [s]	V_{A0} [km s ⁻¹]	B [Gauss]
1	260	10	18	224.19	1640–2319	26–38
2	300	25	25	312.95	1356–1917	22–31

In Table 2 we report the parameters of the loop such as length, inclination, and azimuth angle, the period associated to these loop and the associated Alfvén speed as well as an estimate of the magnetic field. The values agree with those given in the literature.

4. Discussion and conclusions

There are two different oscillation regimes, one with a decayless low-amplitude and one with a decaying high-amplitude, suggesting that the same resonator (the loop) is excited by two different drivers. We modelled the observed oscillations with an externally driven damped-driven oscillator

$$\frac{d^2\xi}{dt^2} + 2\gamma\frac{d\xi}{dt} + \omega_0^2\xi = a_0 e^{-i\omega t} + a_1\delta(t-t_0), \quad (5)$$

where $\xi(t)$ is the transverse displacement of the loop, ω_0 is the natural frequency of the global kink mode ($\omega_0 = C_K\pi/L$, with C_K the kink speed, and L the loop length), γ is the damping rate, e.g. due to resonant absorption. The observations suggest that the oscillation is not over-damped, i.e. $\gamma < \omega_0$. The right-hand side of Eq. (5) contains a continuous low-amplitude harmonic driver of the amplitude a_0 and frequency ω , and an impulsive

driver of the amplitude a_1 at the time t_0 . The driven solution of Eq. (5) is a superposition of the harmonic low-amplitude signal, and an impulsively induced decaying oscillation,

$$\xi(t) = \frac{a_0 \cos(\omega t - \phi)}{\sqrt{(\omega_0^2 - \omega^2)^2 + 4\gamma^2\omega^2}} + a_1 e^{-\gamma(t-t_0)} \cos(\Omega(t-t_0)) H(t-t_0), \quad (6)$$

where $\Omega = \sqrt{|\omega_0^2 - \gamma^2|}$ and $\phi = \tan^{-1}(2\gamma\omega/(\omega_0^2 - \omega^2))$ and $H(x)$ is the Heaviside function. Comparing the empirically determined behaviour of the loop, Eq. (1), with the damped oscillation (6), we obtain that the observed damping time τ does not necessarily match the physical damping time γ^{-1} (Fig. 5-top). It is expected that as the amplitude a_0 increases, the value of τ becomes higher than γ^{-1} because the additional continuous driver will make the impulsively excited oscillation seem to last longer. However, another effect occurs. When the driving and natural frequencies are close, but not too close, a beat is created with a minimum in its envelope within the damping phase of the impulsively oscillation. Thus the observed damping time will be shorter than γ^{-1} . This occurs when

$$0 \leq \frac{\pi - \phi}{\omega - \Omega} \leq s\gamma^{-1} \Leftrightarrow \omega \geq \sqrt{|\omega_0^2 - \gamma^2|} + \frac{\gamma(\pi - \phi)}{s}, \quad (7)$$

where $s\gamma^{-1}$ is the time window in which the oscillation is observed. The exact duration and magnitude of the decrease in the oscillation amplitude depends on the specific values of a_0 , a_1 and γ . Figure 5-bottom shows the decrease in the observed amplitude for short-phase differences between the harmonically and impulsively driven oscillations and for the amplitude ratio $a_0/a_1 \approx 0.5$ (here a_0 represents the full amplitude of the

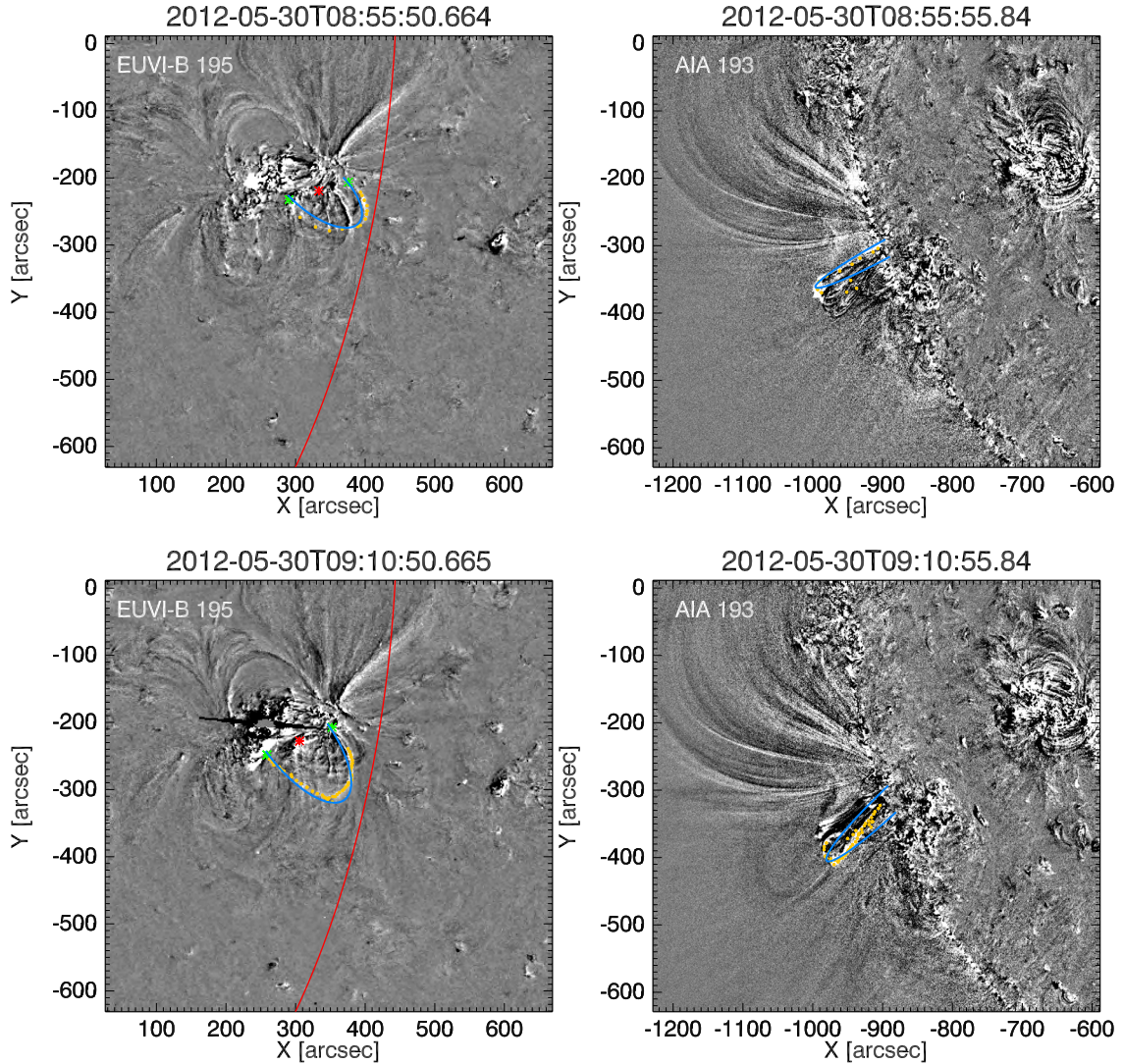


Fig. 4. Three-dimensional reconstruction of two distinct loops before (*top*) and after (*bottom*) the flare, projected on the EUVI-B (*left*) and AIA (*right*) view. We plotted the centre of the loop (red point) on the solar surface, and the footpoints (green points) on the respective sides. The red line in STEREO-B images represents the limb as seen from SDO. The points obtained from the `scc_measure.pro` are plotted as yellow dots and the loop profile is given by a blue line. The movie available on-line shows the temporal evolution of the loops.

driven oscillation, including the square-root denominator). This behaviour is consistent with the one shown in Fig. 3 (middle).

Our observations also showed that the loop gradually expands, which might affect the natural frequency ω_0 . By assuming mass conservation and a constant cross-section of the loop in time, the length L grows by dL , and the mass density ρ decreases as $\rho/(1 + dL/L)$. Since the period of the global kink mode is $P \sim L\rho^{1/2}/B$ (B is the magnetic field), period changes can be written as $P = P_0 + dP = P_0(1 + dL/L)^{1/2}/(1 + dB/B)$, where P_0 is the initial value, in our case $P_0 \sim 215$ s. Indeed, given an increase in height of the loop from 51 to 84 arcsec, and assuming $dB = 0$, the period is expected to be $P = 1.28 P_0 = 275$ s. Moreover, the linear fit of the period measurements (Fig. 3, bottom left) provides an estimate of the growth rate, $m = 0.43$ s/min, leading to a value of $P \sim 280$ s, which is consistent with the expectations.

Therefore, we interpret the observed two regimes of kink oscillations of a coronal loop as the response of the loop (which is a dissipative fast magnetoacoustic resonator) to two different drivers: an external non-resonant harmonic (or possibly,

quasi-harmonic) driver and an impulsive high-amplitude driver. Numerical approaches have been made to study the behaviour of loops in response to periodic or impulsive drivers. Ballai et al. (2008) have found that kink oscillations generated by a harmonic driver have a dominant period belonging to that of the driver, while for a non-harmonic driver (modelling a shock wave) the generated oscillations are of natural periods only. Similar conclusions were reached in Selwa et al. (2010), where the authors pointed out that in the case of an oscillatory driver with a given frequency, only a small subset of loops will start to oscillate, i.e. those whose typical period matches that of the driver. This can be inferred from our time distance maps, where low-amplitude oscillations are sketched for only some loops (e.g. oscillations x_1 , y_1 in Fig. 2), while impulsive excitation generates systematically transverse perturbations in all loops. While the latter is associated with the well-observed flare from STEREO-B, there is no clear association in observations for the former: at the time of decayless oscillations there is no flare energy release. This also excludes the possibility of the excitation by a quasi-monochromatic global coronal wave. Such

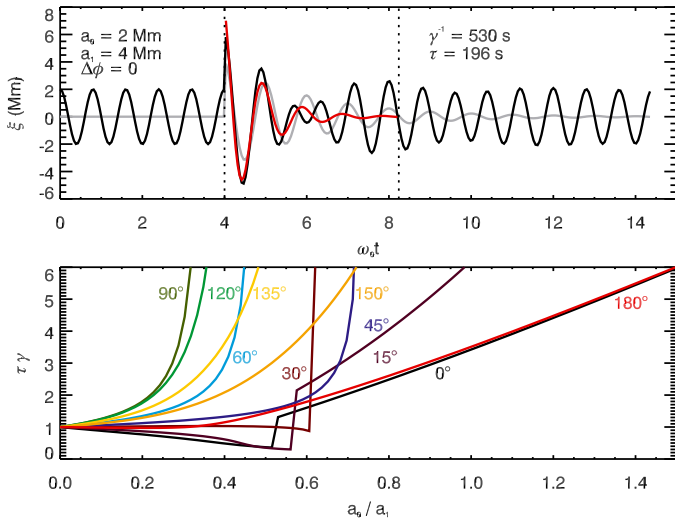


Fig. 5. *Top:* example displacement $\xi(t)$ using Eq. (6) as a function of time, which satisfies condition (7). The amplitudes are $a_0 = 2$ Mm and $a_1 = 4$ Mm. The two oscillations are in phase. The grey curve shows the impulsive part. The red line is the fitted damped oscillation (1). *Bottom:* $\tau\gamma$ as a function of the ratio of amplitudes a_0/a_1 for different phase differences between the two solutions in Eq. (6). Here a_0 represents the full amplitude of the driven oscillation (including the square-root denominator). We assumed $\omega_0 = 2\pi/250$ rad s $^{-1}$, $\omega = 2\pi/200$ rad s $^{-1}$, $\gamma = 1/530$ Hz.

a quasi-periodicity might appear because of dispersion caused by random structuring of the coronal plasma (Nakariakov et al. 2005; Long et al. 2011). The driver responsible for the low-amplitude oscillations before and after the flare should have an intrinsic period of 3–5 min (see period estimates of x_1 , x_2 , and y_1 in Table 1). A possible source can be thought to be the sunspot oscillations, which would be consistent with the empirically established relationship between three min oscillations in solar flares (Sych et al. 2009). However, we cannot use active region magnetograms, because it was still behind the limb. Other driving mechanisms might be unresolved footpoint motions, the effect of granulation, or the effect of periodic Alfvénic vortex shedding caused by the relative motion of the loop with respect to the background plasma. Moreover, the expanding loop we observed and analysed offers us an opportunity to test the validity of theoretical and numerical results. Recently, Ballai & Orza (2012) modelled an expanded coronal loop in an “empty” corona, showing that period and amplitude increase as the length grows (the low-amplitude oscillations analysed by us do not show a consistent increase in the amplitude, which leads us to assume a possible dissipative mechanism in balance with forcing). The approximation of an “empty” corona is very drastic and more efforts are

needed to obtain more realistic results. Our observations in this sense can reveal more about the complex dynamical processes occurring in the solar corona.

Acknowledgements. The data used here are courtesy of the STEREO/SECCHI, SDO (NASA) and AIA consortia. The authors would like to thank the UK-Science and Technology Facilities Council (STFC) for the CFSA Rolling Grant. We also thank the Editors and the anonymous referee for their helpful and constructive comments, which led to significant improvements in the paper.

Note added in proof. Wang et al. (2012) reported growing transverse loop oscillations supposed to be excited from a “continuous non-harmonic” driver, in contrast with our observations. The variety of oscillation events is subject to different interpretations of the possible drivers, which could be obviously ascertained by more detailed observations.

References

- Aschwanden, M. J., Fletcher, L., Schrijver, C. J., & Alexander, D. 1999, *ApJ*, 520, 880
- Ballai, I., & Orza, B. 2012, *A&A*, 545, A118
- Ballai, I., Douglas, M., & Marcu, A. 2008, *A&A*, 488, 1125
- De Moortel, I., & Brady, C. S. 2007, *ApJ*, 664, 1210
- Edwin, P. M., & Roberts, B. 1983, *Sol. Phys.*, 88, 179
- Goossens, M., Andries, J., & Aschwanden, M. J. 2002, *A&A*, 394, L39
- Goossens, M., Andries, J., Soler, R., et al. 2012, *ApJ*, 753, 111
- Handy, B. N., Acton, L. W., Kankelborg, C. C., et al. 1999, *Sol. Phys.*, 187, 229
- Hershaw, J., Foullon, C., Nakariakov, V. M., & Verwichte, E. 2011, *A&A*, 531, A53
- Lemen, J. R., Title, A. M., Akin, D. J., et al. 2012, *Sol. Phys.*, 275, 17
- Long, D. M., DeLuca, E. E., & Gallagher, P. T. 2011, *ApJ*, 741, L21
- McLaughlin, J. A., & Ofman, L. 2008, *ApJ*, 682, 1338
- Murawski, K., & Roberts, B. 1994, *Sol. Phys.*, 151, 305
- Nakariakov, V. M., & Ofman, L. 2001, *A&A*, 372, L53
- Nakariakov, V. M., Ofman, L., DeLuca, E. E., Roberts, B., & Davila, J. M. 1999, *Science*, 285, 862
- Nakariakov, V. M., Pascoe, D. J., & Arber, T. D. 2005, *Space Sci. Rev.*, 121, 115
- Nakariakov, V. M., Aschwanden, M. J., & van Doorselaere, T. 2009, *A&A*, 502, 661
- Pascoe, D. J., Wright, A. N., & De Moortel, I. 2010, *ApJ*, 711, 990
- Roberts, B., Edwin, P. M., & Benz, A. O. 1984, *ApJ*, 279, 857
- Ruderman, M. S., & Roberts, B. 2002, *ApJ*, 577, 475
- Selwa, M., Murawski, K., Solanki, S. K., & Ofman, L. 2010, *A&A*, 512, A76
- Sych, R., Nakariakov, V. M., Karlicky, M., & Anfinogentov, S. 2009, *A&A*, 505, 791
- Terradas, J., Goossens, M., & Verth, G. 2010, *A&A*, 524, A23
- Tomczyk, S., McIntosh, S. W., Keil, S. L., et al. 2007, *Science*, 317, 1192
- Van Doorselaere, T., Nakariakov, V. M., & Verwichte, E. 2007, *A&A*, 473, 959
- Van Doorselaere, T., Nakariakov, V. M., & Verwichte, E. 2008, *ApJ*, 676, L73
- Verth, G., Terradas, J., & Goossens, M. 2010, *ApJ*, 718, L102
- Verwichte, E., Nakariakov, V. M., Ofman, L., & DeLuca, E. E. 2004, *Sol. Phys.*, 223, 77
- Verwichte, E., Nakariakov, V. M., & Cooper, F. C. 2005, *A&A*, 430, L65
- Verwichte, E., Foullon, C., & Van Doorselaere, T. 2010, *ApJ*, 717, 458
- Wang, T., Ofman, L., Davila, J. M., & Su, Y. 2012, *ApJ*, 751, L27
- White, R. S., & Verwichte, E. 2012, *A&A*, 537, A49
- White, R. S., Verwichte, E., & Foullon, C. 2012, *A&A*, 545, A129